

# A deep learning model for chemical shieldings in molecular organic solids including anisotropy

Matthias Kellner,<sup>1</sup> Jacob B. Holmes,<sup>2</sup> Ruben Rodriguez-Madrid,<sup>2</sup> Florian Viscosi,<sup>2</sup> Yuxuan Zhang,<sup>1</sup> Lyndon Emsley,<sup>2</sup> and Michele Ceriotti<sup>1,\*</sup>

<sup>1</sup>Laboratory of Computational Science and Modeling, Institut des Matériaux, École Polytechnique Fédérale de Lausanne, 1015 Lausanne, Switzerland

<sup>2</sup>Laboratory of Magnetic Resonance, Institut des Sciences et Ingénierie Chimiques, École Polytechnique Fédérale de Lausanne, 1015 Lausanne, Switzerland

(Dated: June 17, 2025)

Nuclear Magnetic Resonance (NMR) chemical shifts are powerful probes of local atomic and electronic structure that can be used to resolve the structures of powdered or amorphous molecular solids. Chemical shift driven structure elucidation depends critically on accurate and fast predictions of chemical shieldings, and machine learning (ML) models for shielding predictions are increasingly used as scalable and efficient surrogates for demanding ab initio calculations. However, the prediction accuracies of current ML models still lag behind those of the DFT reference methods they approximate, especially for nuclei such as  $^{13}\text{C}$  and  $^{15}\text{N}$ . Here, we introduce ShiftML3, a deep-learning model that improves the accuracy of predictions of isotropic chemical shieldings in molecular solids, and does so while also predicting the full shielding tensor. On experimental benchmark sets, we find root-mean-squared errors with respect to experiment for ShiftML3 that approach those of DFT reference calculations, with RMSEs of 0.53 ppm for  $^1\text{H}$ , 2.4 ppm for  $^{13}\text{C}$ , and 7.2 ppm for  $^{15}\text{N}$ , compared to DFT values of 0.49 ppm, 2.3 ppm, and 5.8 ppm, respectively.

Chemical function is directly related to structure. As a result, the determination of atomic-level three-dimensional structures is at the heart of molecular and materials science. In this context, solid-state NMR (often in conjunction with diffraction methods and other spectroscopic methods) has emerged as the method of choice for atomic-level characterization of complex materials in powder form. This has been driven by the development of methods to probe the local atomic environment based on chemical shifts, [1–6] often referred to as NMR crystallography. In turn, this has been made possible by the development of accurate density functional theory (DFT) based methods to calculate chemical shifts. [7, 8] Indeed, it has been recently shown that NMR can elucidate structures of molecular solids from powders with resolution better than 0.2 Å. [9, 10]

In a nutshell, NMR crystallography consists in experimentally measuring and assigning chemical shifts for each of the atomic sites in a structure, and then comparing the measured shifts to those predicted by computation for a pool of candidate structures, that are themselves enumerated by a computational search. Chemical shifts are traditionally calculated using DFT methods. [7, 11–14] This workflow has been successful for materials ranging from hybrid-perovskites [15, 16] and inorganic materials [17–22] to enzyme activate sites, [10, 23, 24] organic molecular solids, [25–39] and notably for amorphous drug formulations. [40–43] One of the key bottlenecks to address in this workflow is both the computational cost and the accuracy of chemical shift predictions.

The introduction of accurate machine learning models to predict chemical shifts in solids has essentially removed the computational cost barrier, allowing for

tens of millions of shifts to be predicted on the order of days. [44–53] For organic molecular solids, Paruzzo *et al.* [45] developed a model (dubbed ShiftML) that could predict isotropic chemical shifts for any molecular solid containing C, H, N, O atoms, that was trained on GIPAW DFT data for 2,000 structures from the Cambridge structural database (CSD). [54] Engel and coworkers later broadened its applicability to sulfur-containing compounds. [55] The model was subsequently improved and extended to ShiftML2 [49] which was trained on an extended set of over 14,000 structures containing H, C, N, O, S, F, P, Cl, Na, Ca, Mg and K, and composed of both relaxed and thermally perturbed structures. Both ShiftML models used kernel ridge regression (KRR), [56] with uncertainties in the predictions estimated using a committee of 32 models (for ShiftML2). [57] The local atomic environments were described using smooth overlap of atomic positions (SOAP) descriptors. [58]

The predictions of ShiftML2 yield an accuracy for isotropic  $^1\text{H}$  shifts of 0.5 ppm with respect to the DFT computed shifts, and an accuracy of 0.47 ppm with respect to a benchmark set of experimental shifts. [49] Increasing the accuracy of shift prediction for ML models would directly translate to better structure determination. Indeed, Unzueta *et al.* [48] have shown that using a  $\Delta$ -ML approach to improve the prediction accuracy of DFT computed shifts themselves, by correcting the effects of small basis set sizes in DFT shielding calculations, can lead to errors as small as 0.11 ppm for  $^1\text{H}$  shifts with respect to DFT. Although this is not directly relevant to pure ML predictions, since they use DFT computations as a starting point, it does nicely illustrate the potential to develop more accurate models.

Even though DFT calculations naturally yield the full chemical shielding tensor, the prediction models developed so far for molecular solids were only trained on isotropic values of the chemical shift (where the isotropic shift is the average of the three principal components). Recently, models for silicon oxides [51, 52] and non-magnetic oxides [53] have been introduced to predict the full chemical shift tensor with orientation, extending the scope of ML-predicted chemical shieldings to applications that rely on the chemical shift anisotropy (CSA). Tensorial models have also been used to predict other quantities relevant to nuclear spectroscopy, such as electric field gradients [59] and zero-field splitting tensors [60].

Here, we present a new machine learning model (dubbed ShiftML3) that predicts the full chemical shielding tensors, trained using shieldings calculated at the GIPAW/PBE level of theory. The model is based on an ensemble of *Point Edge Transformer* (PET) models. [61] The model not only predicts anisotropic shieldings, but also yields significantly improved accuracy with respect to DFT, with up to a two-fold improvement over ShiftML2 for the isotropic shieldings of heavy atoms.

Isotropic shifts are often sufficient to identify the experimentally-observed crystal structure out of a pool of potential candidates. For this reason, previous ShiftML models have been constructed by directly learning the isotropic chemical shieldings  $\sigma_{\text{iso}}$  from DFT calculations, using symmetry-adapted models designed to make predictions that are exactly invariant to rigid rotations of a structure. However, the chemical shielding is a tensorial property, whose anisotropy (typically referred to as the chemical shift anisotropy or CSA) provides additional information that can be useful to explore crystal structures. [62] Given that GIPAW-DFT calculations yield the full chemical shielding tensor, in ShiftML3 we include tensorial predictions, focusing on the symmetric component which is of experimental relevance. For molecular solids, isotropic chemical shifts are readily measured using fast magic-angle spinning (MAS) methods, [4] and CSA can be measured using slow MAS [63] or using multi-dimensional isotropic-anisotropic correlation experiments to avoid spectral crowding. [64–67] While these parameters are readily measurable, there is currently no sufficiently large database of experimental shifts for molecular solids with corresponding high-resolution atomic-level structures. This is in contrast to small molecules and proteins in solution, which have large and well-curated experimental databases. [68, 69] As a result, ML models in solids have been developed by using curated sets of structures together with shifts computed using DFT.

Here we use the training set from the most recent previous ShiftML model, and for which the computed shifts (computed at the PBE level of theory) contain the full tensor information. [49] This dataset is composed of molecular solids where the structures include (up to) 12

elements [H, C, N, O, F, Na, Mg, P, S, Cl, K, Ca] commonly found in organic compounds. It contains a total of 14,146 structures, including 7,548 sampled from the Cambridge structural database (CSD) via farthest point sampling (FPS) [70] to cover a broad range of structural motifs, and 6,598 additional thermally distorted structures. The ShiftML2 test set was divided into a new validation (505 structures, with 41,599 atomic environments) and a new test set (1,254 structures, with 106,230 atomic environments). In this split we choose a stratified selection strategy that ensures that both the distorted and the relaxed structure of any one CSD identifier are found either in the validation or the test set, avoiding data leakage between the sets. Furthermore, we ensure that both the new validation and new test sets contain at least a few environments of all 12 chemical elements. To compare the accuracies between ShiftML2 and ShiftML3 in a consistent fashion, the accuracies are reported on this new test set (referred to as the *CSD-test* set). More details of the training, validation and test sets for each element in *CSD-test* are given in section S1 of the supporting information. Due to computational constraints, ShiftML2 was trained on a representative subselection of atomic environments from the training set. The favorable computational scaling of neural network training via stochastic gradient descent allowed us to train ShiftML3 using all 1.4 million atomic environments contained in the 14,146 structures in the training set. The updated dataset containing the chemical shielding tensor data is available via a public data record associated with this publication. [71] We also use established datasets of experimental isotropical chemical shielding values, with 13 structures for  $^1\text{H}$ , 21 for  $^{13}\text{C}$ , and 15 for  $^{15}\text{N}$ , [14, 49] and a benchmark set of experimental  $^{13}\text{C}$  CSA principal values for 19 compounds. [72]

For the construction of the ShiftML3 model, we learn the correlation between chemical shielding tensor and structure using an ensemble of *Point Edge Transformer* (PET) models. [61] PET is an unconstrained graph neural network (GNN) architecture that delivers accurate and fast predictions for several material properties benchmark sets, importantly also on rotationally equivariant targets such as molecular dipole moments. [61] For ShiftML3, we use a modified version of the PET architecture referred to as nanoPET (available via the *metatrain* library). [73] Even though nanoPET does not enforce rotational invariance or equivariance of the target predictions, it learns the rotational behaviour of the targets via rotational augmentation during the training process – a mechanism that has been shown to yield models that are symmetry-compliant to a high accuracy. [74]

In practice, nanoPET predicts the chemical shielding tensors in their irreducible spherical tensor (IST) representation in a manner similar to symmetry-adapted, rotationally-constrained models. [75] The chemical shielding tensors are decomposed into their irre-

ducible real spherical representations: A scalar,  $\lambda = 0$  part, a  $\lambda = 1$  pseudovector, and a  $\lambda = 2$  proper 5-vector having the same rotational behaviour as their corresponding  $Y^\lambda$  spherical harmonics. [76] We refer the reader to the following references, [77–79] for a more in depth discussion of the properties of the chemical shielding tensor and a discussion of its rotational properties. nanoPET uses a single message-passing sequence of unconstrained graph transformer modules, with one final linear readout layer per IST component,  $T^\lambda$ . The final tensor predictions are then obtained by a change of representation back from the predicted IST components to the tensor in the Cartesian basis.

During the training procedure, random rotations in their irreducible Wigner-D matrix representations are automatically applied to the target IST components at each training step, as well as random inversions. We train an ensemble consisting of 8 nanoPET models. The models are trained for 1,500 epochs, with a constant learning rate of  $3 \cdot 10^{-4}$ . We train the model using mini batch gradient descent with the Adam optimizer [80] and a batch size of 4. The construction of an ensemble model has several benefits; in addition to increased prediction accuracies, an ensemble also provides uncertainty estimates and further reduces the rotational symmetry breaking of the nanoPET predictions. [81, 82] In Section S2 of the supporting information we make a detailed assessment of the residual symmetry errors of the ShiftML3 model.

When performing hyperparameter optimization we observed that the prediction accuracies of individual nanoPET models do not vary strongly between reasonable guesses of potential hyperparameter choices (cutoffs, number of message passing layers and token size). We therefore employ a set of hyperparameters for the nanoPET implementation that provides a good compromise between accuracy and evaluation speed. An in-depth evaluation of the computational speed of the ShiftML3 model can be found in the section S3 of the supporting information. We choose a radial cutoff of 5 Å to encode local information (displacement vectors, atom types and messages from neighbouring atoms) into tokens. ShiftML3 employs 2 message passing layers and 2 attention layers per message passing step, and a token dimensionality of 192. For better usability, we make ShiftML3 available through a Python package (more information in section S4 of the supporting information).

The predictions are affected by a structure-dependent uncertainty, which should be quantified to assess how reliably the model can be used for a structure determination task – especially to identify the degradation of accuracy that usually occurs in the extrapolative regime. In many cases the uncertainty can be attributed to lack of knowledge of the model due to improper sampling of the training data (epistemic uncertainties). [83] Here, we refer to the prediction accuracy of the model with respect to the DFT calculations, whereas the underlying error of the

electronic-structure reference would need to be assessed by comparison with experiments or higher-level calculations.

PET and most other atomistic neural networks make only point estimates of the target quantity. Constructing an ensemble is a universal strategy to equip ML models with uncertainty estimates, [84, 85] even if the model does not allow for a probabilistic interpretation of its predictions. An ensemble model is constructed by training multiple models. The final prediction for an atomic local environment,  $A_i$ , of an ensemble of  $N_{ens}$  models, is then taken to be the mean of the individual predictions of the “committee” members,  $\bar{y}(A_i)$ , and their spread is taken to be an indicator of the reliability of the model predictions:

$$\sigma_{\text{pred}}^2(A_i) = \frac{1}{N_{\text{ens}} - 1} \sum_{k=1}^{N_{\text{ens}}} [y^k(A_i) - \bar{y}(A_i)]^2 \quad (1)$$

We compute uncertainty estimates from the committee of PET model predictions. We note in passing that it is often possible to reduce the overhead of ensemble models by building *shallow ensembles* that share the time-consuming part of the evaluation, and differ only by their last-layer features. [86] Here we opt for a full ensembling to maximise prediction accuracies in line with previous works on prediction chemical shieldings with deep learning networks. [46, 87] Following standard practice, [88, 89] we calibrate the uncertainty estimates of ShiftML3 on the validation set, scaling the predicted ensemble uncertainties with a global, input-independent correction. [57] More details of the model calibration and evaluation of the uncertainty estimates can be found in section S5 of the supporting information.

To evaluate the performance of ShiftML3, we first compare predicted isotropic chemical shieldings against DFT calculated isotropic shieldings on the *CSD-test* set. Figure 1 shows parity plots illustrating the overall agreement between ShiftML3 and DFT with an RMSE of 0.43 ppm, 2.3 ppm and 10.4 ppm for  $^1\text{H}$ ,  $^{13}\text{C}$  and  $^{15}\text{N}$ , respectively. These correspond to an error reduction between 20% to a factor of 2 relative to ShiftML2. Similar levels of improvement are seen also for almost all nuclei represented in the dataset, as shown in Table I (with the exception of  $^{39}\text{K}$ , for which there are only 6 atomic environments in the test set, making the assessment inconclusive).

We then evaluate the chemical shielding tensor predictions of the ShiftML3 model on the *CSD-test* set, and report the prediction accuracies of symmetric tensor components in Table II. More information, including parity plots for  $^{13}\text{C}$  and  $^{15}\text{N}$  anisotropic shieldings can be found in section S6 of the supporting information. We report prediction accuracies for the combined principal components  $\sigma_{\text{PAS}}$  and combined tensor components  $\sigma_{ij}$ . We report averaged prediction errors over all tensor components or principal components and across atomic envi-

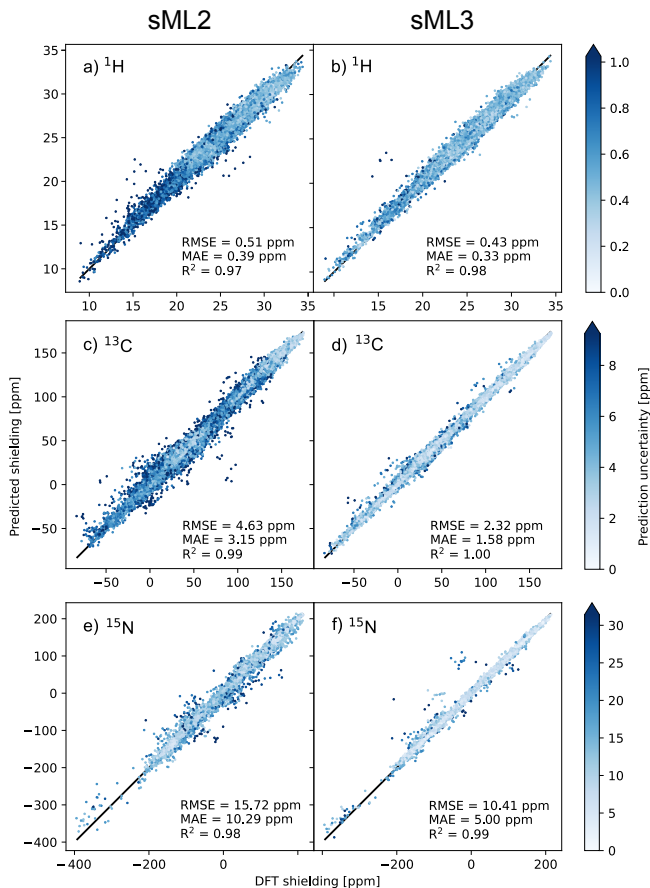


Figure 1: Parity plots between DFT-computed shieldings and predictions using ShiftML2 or ShiftML3 for (a,b)  $^1\text{H}$ , (c,d)  $^{13}\text{C}$  and (e,f)  $^{15}\text{N}$  evaluated on the new *CSD-test* set. The black line shows perfect correlation while the colour each point is correlated to the prediction uncertainty of that atomic site. Each point is colored according to the rescaled prediction uncertainty associated in each atomic site.

ronments in the test dataset, consistent with the error metric reported for chemical shieldings, which themselves are the average of the three principal components of the chemical shielding tensor. We obtain averaged eigenvalues of the ensemble, by first computing the eigendecomposition of the individual committee member predictions and then averaging over the committee prediction of principal components.

The improvements in prediction accuracy against the DFT reference also translate to an increased accuracy of ShiftML predictions against experiments. We find that on a representative benchmark set of experimentally measured  $^1\text{H}$  and  $^{13}\text{C}$  shieldings, [14, 49] ShiftML3 predicts chemical shieldings with accuracies almost on par with GIPAW DFT, namely: 0.53(0.49) ppm for  $^1\text{H}$  and 2.4(2.3) ppm for  $^{13}\text{C}$ , for ShiftML3(DFT). Figure 2,

Table I: Prediction accuracies of ShiftML2 (sML2) and ShiftML3 (sML3) models on the *CSD-test* dataset. MAE and RMSE (in ppm) are evaluated on a hold-out test set.

nucleus	MAE		RMSE		$R^2$	
	sML2	sML3	sML2	sML3	sML2	sML3
$^1\text{H}$	0.39	0.33	0.51	0.43	0.97	0.98
$^{13}\text{C}$	3.15	1.58	4.63	2.32	0.99	1.00
$^{15}\text{N}$	10.29	5.00	15.72	10.41	0.98	0.99
$^{17}\text{O}$	16.11	7.51	22.96	11.45	0.98	1.00
$^{19}\text{F}$	7.77	4.42	10.83	6.66	0.97	0.99
$^{33}\text{S}$	34.35	15.05	53.34	26.34	0.88	0.97
$^{31}\text{P}$	21.83	9.49	39.20	18.98	0.62	0.91
$^{35}\text{Cl}$	17.40	10.44	23.85	15.11	0.96	0.98
$^{23}\text{Na}$	7.64	4.09	8.10	4.61	0.00	0.68
$^{43}\text{Ca}$	5.81	2.96	6.98	3.34	0.81	0.96
$^{25}\text{Mg}$	10.69	3.68	14.55	5.49	0.66	0.95
$^{39}\text{K}$	3.42	4.29	4.28	4.65	0.77	0.73

Table II: Prediction accuracies of ShiftML3 on symmetric tensor components  $\sigma_{ij}$  and principal tensor components  $\sigma_{\text{PAS}}$ . MAE and RMSE (in ppm) are evaluated on a hold-out test set.

nucleus	$\sigma_{ij}$			$\sigma_{\text{PAS}}$		
	MAE	RMSE	$R^2$	MAE	RMSE	$R^2$
$^1\text{H}$	0.54	0.72	1.00	0.65	0.85	0.98
$^{13}\text{C}$	2.10	3.08	1.00	2.64	3.88	1.00
$^{15}\text{N}$	5.32	10.75	0.99	7.21	15.62	0.99
$^{17}\text{O}$	7.58	12.09	0.99	10.28	16.79	1.00
$^{19}\text{F}$	4.05	6.28	1.00	5.73	8.65	0.99
$^{33}\text{S}$	17.15	30.37	0.97	22.53	42.73	0.97
$^{31}\text{P}$	10.30	18.73	0.98	13.35	23.59	0.95
$^{35}\text{Cl}$	10.14	15.32	1.00	14.02	20.50	0.99
$^{23}\text{Na}$	2.83	4.01	1.00	4.28	5.24	0.91
$^{43}\text{Ca}$	3.14	3.85	1.00	4.53	4.93	0.98
$^{25}\text{Mg}$	7.48	9.79	1.00	6.27	8.34	0.93
$^{39}\text{K}$	2.93	3.95	1.00	4.42	5.21	0.87

shows parity plots of isotropic chemical shieldings estimated with ShiftML2, ShiftML3 and DFT with respect to experimental chemical shifts. DFT values were evaluated recomputing the NMR shieldings using GIPAW [7] on the the Quantum ESPRESSO software [90, 91] with the same DFT parameters as in Ref. 49. The conversion between experimental chemical shifts and predicted shieldings is performed by fitting globally the shieldings across all test compounds to a linear form, also shown in figure 2. Further details about the experimental benchmark are discussed in section S7 of the supporting information.

We also assess the accuracy of the CSA predictions against experiments, based on a benchmark of  $^{13}\text{C}$  shieldings for a set of structures whose experimental shifts had

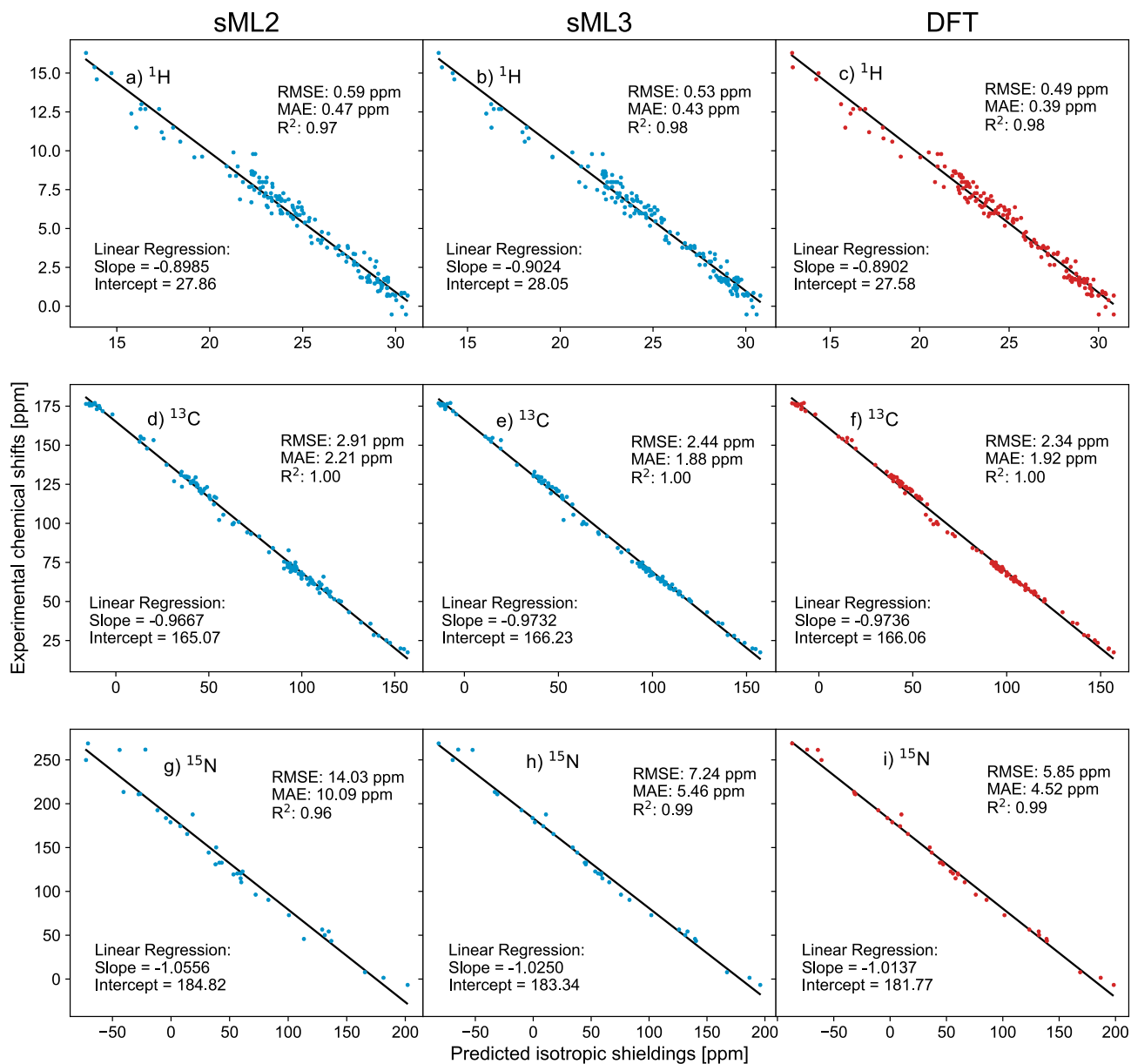


Figure 2: Parity plots between experimental chemical shifts and predictions from ShiftML2, ShiftML3 and DFT calculations for (a,b,c) <sup>1</sup>H, (d, e, f) <sup>13</sup>C, and (g, h, i) <sup>15</sup>N evaluated on the benchmark structures from Ramos *et al.* [14] for <sup>13</sup>C and <sup>15</sup>N, and the 13 structures where ShiftML2 was evaluated for <sup>1</sup>H. The black line shows the linear regression between experimental chemical shifts and predicted isotropic shieldings with their slope and intercept indicated in each respective subplot.

been reported in Ref. 72. The accuracy in terms of the three principal components ( $\sigma_{11}, \sigma_{22}, \sigma_{33}$ ) of the shielding tensor is on par with that of DFT. The RMSE of for ShiftML3 (5.2 ppm) is even smaller than for DFT (5.8 ppm) which is likely fortuitous (Fig. 3).

Overall, we find that the improved accuracy of ShiftML3 against DFT-computed isotropic shieldings, relative to ShiftML2, is reflected in a corresponding improvement of the match with experiments, that is now

essentially limited by the accuracy of the reference DFT calculations. The tensorial predictions also have a DFT-level match with experiments, providing a further diagnostic to support structure determination and provide mechanistic insights.

To summarize our findings, we have presented a machine learning model for the prediction of chemical shieldings in organic crystals, using an unconstrained graph neural network architecture that delivers chemical shield-

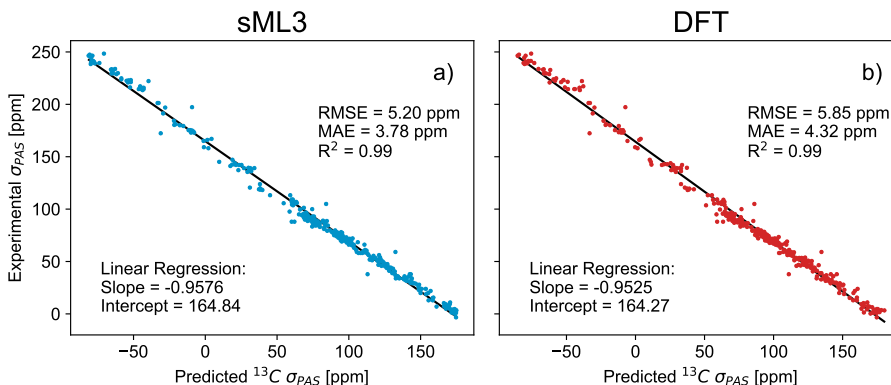


Figure 3: Parity plots between experimental principal components  $\sigma_{PAS}$  of the CSA tensor and predicted components using ShiftML3 for the CSA components evaluated on a subset of benchmark structures from Ramos *et al.* [14]. The black line shows the linear regression between experimental and predicted CSA principal components, with their slope and intercept shown in each respective subplot.

ing tensors and uncertainty quantification through an ensemble structure. We have shown that across all nuclei that are well-represented in the dataset, ShiftML3 predicts accurate shielding tensors and isotropic shieldings in organic crystals. The isotropic prediction RMSE of 0.43 ppm for  $^1\text{H}$  and 2.3 ppm for  $^{13}\text{C}$  against GIPAW reference calculations are a major improvement over previous ShiftML versions based on symmetry-adapted kernel models. The improved prediction accuracies translate to an accuracy against experimental benchmarks that practically matches that of DFT calculations, improving the confidence of NMR-guided structural determination. The availability of chemical shieldings anisotropy, with an accuracy that also approaches that of DFT, facilitates comparison with other types of NMR experiments, providing structural and mechanistic insights. The easy-to-use, fast, and openly-available implementation will facilitate usage for a broad community interested in the theoretical and experimental study of organic materials by means of NMR.

## ACKNOWLEDGEMENTS

We thank Filippo Bigi and Michelangelo Domina for assistance with their nanoPET-IST implementation and Sergey Pozdnyakov for adapting the original PET architecture for isotropic shieldings. We thank Joseph William Abbott for the provision of a  $\lambda$ -SOAP model, which we used to prototype chemical shielding anisotropy predictions. This work has been supported by Swiss National Science Foundation Grant No. 200020\_212046, and by the NCCR MARVEL, funded by the Swiss National Science Foundation (grant number 182892). MC also acknowledged funding from the ERC Horizon 2020 Grant No. 101001890-FIAMMA.

## SUPPORTING INFORMATION

The supporting information is provided below, containing additional details on dataset and model construction, uncertainty quantification, and the usage of the ShiftML3 Python package, which is available under an open source license at <https://github.com/lab-cosmo/shiftml>. The training, validation and testing datasets containing chemical shielding tensor data as well as training input files, model files and evaluation scripts will be made available upon publication via the public data record associated with this publication. [71]

\* michele.cerioti@epfl.ch

- [1] D. D. Laws, H.-M. L. Bitter, and A. Jerschow, *Solid-State NMR Spectroscopic Methods in Chemistry*, *Angewandte Chemie International Edition* **41**, 3096 (2002).
- [2] S. E. Ashbrook and D. McKay, *Combining solid-state NMR spectroscopy with first-principles calculations – a guide to NMR crystallography*, *Chemical Communications* **52**, 7186 (2016).
- [3] P. Hodgkinson, *NMR crystallography of molecular organics*, *Progress in Nuclear Magnetic Resonance Spectroscopy* **118–119**, 10 (2020).
- [4] B. Reif, S. E. Ashbrook, L. Emsley, and M. Hong, *Solid-state NMR spectroscopy*, *Nature Reviews Methods Primers* **1**, 2 (2021).
- [5] L. Emsley, *Spiers Memorial Lecture: NMR crystallography*, *Faraday Discussions* **255**, 9 (2025).
- [6] D. L. Bryce, *Modern NMR Crystallography: Concepts and Applications* (Royal Society of Chemistry, 2025).
- [7] C. J. Pickard and F. Mauri, *All-electron magnetic response with pseudopotentials: NMR chemical shifts*, *Physical Review B* **63**, 245101 (2001).
- [8] J. D. Hartman, R. A. Kudla, G. M. Day, L. J. Mueller, and G. J. O. Beran, *Benchmark fragment-based  $^1\text{H}$ ,  $^{13}\text{C}$ ,  $^{15}\text{N}$  and  $^{17}\text{O}$  chemical shift predictions in molecular*

- crystals, *Physical Chemistry Chemical Physics* **18**, 21686 (2016).
- [9] A. Hofstetter and L. Emsley, Positional Variance in NMR Crystallography, *Journal of the American Chemical Society* **139**, 2573 (2017).
- [10] J. B. Holmes, V. Liu, B. G. Caulkins, E. Hilario, R. K. Ghosh, V. N. Drago, R. P. Young, J. A. Romero, A. D. Gill, P. M. Bogie, J. Paulino, X. Wang, G. Riviere, Y. K. Bosken, J. Struppe, A. Hassan, J. Guidoulianov, B. Perrone, F. Mentink-Vigier, C.-e. A. Chang, J. R. Long, R. J. Hooley, T. C. Mueser, M. F. Dunn, and L. J. Mueller, Imaging active site chemistry and protonation states: NMR crystallography of the tryptophan synthase  $\alpha$ -aminoacrylate intermediate, *Proceedings of the National Academy of Sciences* **119**, e2109235119 (2022).
- [11] J. R. Yates, C. J. Pickard, and F. Mauri, Calculation of NMR chemical shifts for extended systems using ultrasoft pseudopotentials, *Physical Review B* **76**, 024401 (2007).
- [12] C. Bonhomme, C. Gervais, F. Babonneau, C. Coelho, F. Pourpoint, T. Azaïs, S. E. Ashbrook, J. M. Griffin, J. R. Yates, F. Mauri, and C. J. Pickard, First-Principles Calculation of NMR Parameters Using the Gauge Including Projector Augmented Wave Method: A Chemist's Point of View, *Chemical Reviews* **112**, 5733 (2012).
- [13] G. J. O. Beran, Modeling Polymorphic Molecular Crystals with Electronic Structure Theory, *Chemical Reviews* **116**, 5567 (2016).
- [14] S. A. Ramos, L. J. Mueller, and G. J. O. Beran, The interplay of density functional selection and crystal structure for accurate NMR chemical shift predictions, *Faraday Discussions*, 10.1039.D4FD00072B (2024).
- [15] M. A. Hope, T. Nakamura, P. Ahlawat, A. Mishra, M. Cordova, F. Jahanbakhshi, M. Mladenović, R. Runjhun, L. Merten, A. Hinderhofer, B. I. Carlsen, D. J. Kubicki, R. Gershoni-Poranne, T. Schneeberger, L. C. Carbone, Y. Liu, S. M. Zakeeruddin, J. Lewinski, A. Hagfeldt, F. Schreiber, U. Rothlisberger, M. Grätzel, J. V. Milić, and L. Emsley, Nanoscale Phase Segregation in Supramolecular  $\pi$ -Templating for Hybrid Perovskite Photovoltaics from NMR Crystallography, *Journal of the American Chemical Society* **143**, 1529 (2021).
- [16] D. J. Kubicki, S. D. Stranks, C. P. Grey, and L. Emsley, NMR spectroscopy probes microstructure, dynamics and doping of metal halide perovskites, *Nature Reviews Chemistry* **5**, 624 (2021).
- [17] J. Senker, J. Sehnert, and S. Correll, Microscopic Description of the Polyamorphic Phases of Triphenyl Phosphite by Means of Multidimensional Solid-State NMR Spectroscopy, *Journal of the American Chemical Society* **127**, 337 (2005).
- [18] S. K. Lee, S. Y. Park, Y. S. Yi, and J. Moon, Structure and Disorder in Amorphous Alumina Thin Films: Insights from High-Resolution Solid-State NMR, *The Journal of Physical Chemistry C* **114**, 13890 (2010).
- [19] P. Gras, A. Baker, C. Combes, C. Rey, S. Sarda, A. J. Wright, M. E. Smith, J. V. Hanna, C. Gervais, D. Laurencin, and C. Bonhomme, From crystalline to amorphous calcium pyrophosphates: A solid state Nuclear Magnetic Resonance perspective, *Acta Biomaterialia* **31**, 348 (2016).
- [20] B. Walkley and J. Provis, Solid-state nuclear magnetic resonance spectroscopy of cements, *Materials Today Advances* **1**, 100007 (2019).
- [21] A. Kunhi Mohamed, P. Moutzouri, P. Berruyer, B. J. Walder, J. Siramanont, M. Harris, M. Negroni, S. C. Galmarini, S. C. Parker, K. L. Scrivener, L. Emsley, and P. Bowen, The Atomic-Level Structure of Cementitious Calcium Aluminate Silicate Hydrate, *Journal of the American Chemical Society* **142**, 11060 (2020).
- [22] A. Morales-Melgares, Z. Casar, P. Moutzouri, A. Venkatesh, M. Cordova, A. Kunhi Mohamed, K. L. Scrivener, P. Bowen, and L. Emsley, Atomic-Level Structure of Zinc-Modified Cementitious Calcium Silicate Hydrate, *Journal of the American Chemical Society* **144**, 22915 (2022).
- [23] H. Singh, S. K. Vasa, H. Jangra, P. Rovó, C. Päslock, C. K. Das, H. Zipse, L. V. Schäfer, and R. Linser, Fast Microsecond Dynamics of the Protein–Water Network in the Active Site of Human Carbonic Anhydrase II Studied by Solid-State NMR Spectroscopy, *J. Am. Chem. Soc.* (2019).
- [24] A. Bertarello, L. Benda, K. J. Sanders, A. J. Pell, M. J. Knight, V. Pelmeshnikov, L. Gonnelli, I. C. Felli, M. Kaupp, L. Emsley, R. Pierattelli, and G. Pintacuda, Picometer Resolution Structure of the Coordination Sphere in the Metal-Binding Site in a Metalloprotein by NMR, *Journal of the American Chemical Society* **142**, 16757 (2020).
- [25] D. A. Middleton, C. S. Le Duff, X. Peng, D. G. Reid, and D. Saunders, Molecular Conformations of the Polymorphic Forms of Cimetidine from  $^{13}\text{C}$  Solid-State NMR Distance and Angle Measurements, *Journal of the American Chemical Society* **122**, 1161 (2000).
- [26] J. R. Yates, S. E. Dobbins, C. J. Pickard, F. Mauri, P. Y. Ghi, and R. K. Harris, A combined first principles computational and solid-state NMR study of a molecular crystal: Flurbiprofen, *Physical Chemistry Chemical Physics* **7**, 1402 (2005).
- [27] R. K. Harris, S. A. Joyce, C. J. Pickard, S. Cadars, and L. Emsley, Assigning carbon-13 NMR spectra to crystal structures by the INADEQUATE pulse sequence and first principles computation: A case study of two forms of testosterone, *Phys. Chem. Chem. Phys.* **8**, 137 (2006).
- [28] R. K. Harris, S. Cadars, L. Emsley, J. R. Yates, C. J. Pickard, R. K. R. Jetti, and U. J. Griesser, NMR crystallography of oxybuprocaine hydrochloride, Modification II $^\circ$ , *Phys. Chem. Chem. Phys.* **9**, 360 (2007).
- [29] E. Salager, G. M. Day, R. S. Stein, C. J. Pickard, B. Elena, and L. Emsley, Powder Crystallography by Combined Crystal Structure Prediction and High-Resolution  $^1\text{H}$  Solid-State NMR Spectroscopy, *Journal of the American Chemical Society* **132**, 2564 (2010).
- [30] R. K. Harris, P. Hodgkinson, V. Zorin, J.-N. Dumez, B. Elena-Herrmann, L. Emsley, E. Salager, and R. S. Stein, Computation and NMR crystallography of terbutaline sulfate, *Magnetic Resonance in Chemistry* **48**, S103 (2010).
- [31] M. Baias, C. M. Widdifield, J.-N. Dumez, H. P. G. Thompson, T. G. Cooper, E. Salager, S. Bassil, R. S. Stein, A. Lesage, G. M. Day, and L. Emsley, Powder crystallography of pharmaceutical materials by combined crystal structure prediction and solid-state  $^1\text{H}$  NMR spectroscopy, *Physical Chemistry Chemical Physics* **15**, 8069 (2013).
- [32] M. Baias, J.-N. Dumez, P. H. Svensson, S. Schantz, G. M. Day, and L. Emsley, *De Novo* Determination of the Crystal Structure of a Large Drug Molecule by Crystal Structure Prediction-Based Powder NMR Crystallog-

- raphy, *Journal of the American Chemical Society* **135**, 17501 (2013).
- [33] A. C. Pinon, A. J. Rossini, C. M. Widdifield, D. Gagan, and L. Emsley, Polymorphs of Theophylline Characterized by DNP Enhanced Solid-State NMR, *Molecular Pharmaceutics* **12**, 4146 (2015).
- [34] E. Pindelska, L. Szeleszczuk, D. M. Pisklak, A. Mazurek, and W. Kolodziejewski, Solid-State NMR as an Effective Method of Polymorphic Analysis: Solid Dosage Forms of Clopidogrel Hydrogensulfate, *Journal of Pharmaceutical Sciences* **104**, 106 (2015).
- [35] C. A. Rezende, R. A. San Gil, L. B. Borré, J. R. Pires, V. S. Vaiss, J. A. Resende, A. A. Leitão, R. B. De Alencastro, and K. Z. Leal, Combining Nuclear Magnetic Resonance Spectroscopy and Density Functional Theory Calculations to Characterize Carvedilol Polymorphs, *Journal of Pharmaceutical Sciences* **105**, 2648 (2016).
- [36] Y. Tian, W. D. Wang, W.-B. Zou, J.-Q. Qian, and C.-Q. Hu, Application of Solid-State NMR to Reveal Structural Differences in Cefazolin Sodium Pentahydrate From Different Manufacturing Processes, *Frontiers in Chemistry* **6**, 113 (2018).
- [37] L. Szeleszczuk, D. M. Pisklak, T. Gubica, K. Matjakowska, S. Kaźmierski, and M. Zielińska-Pisklak, Application of combined solid-state NMR and DFT calculations for the study of piracetam polymorphism, *Solid State Nuclear Magnetic Resonance* **97**, 17 (2019).
- [38] Y. Dai, V. Terskikh, A. Brinckmann, and G. Wu, Solid-State  $^1\text{H}$ ,  $^{13}\text{C}$ , and  $^{17}\text{O}$  NMR Characterization of the Two Uncommon Polymorphs of Curcumin, *Crystal Growth & Design* **20**, 7484 (2020).
- [39] SA. Southern and DL. Bryce, *Annual Reports on NMR Spectroscopy*, Webb GA, Ed **102**, 1 (2021).
- [40] M. Cordova, M. Balodis, A. Hofstetter, F. Paruzzo, S. O. Nilsson Lill, E. S. E. Eriksson, P. Berruyer, B. Simões De Almeida, M. J. Quayle, S. T. Norberg, A. Svensk Ankarberg, S. Schantz, and L. Emsley, Structure determination of an amorphous drug through large-scale NMR predictions, *Nature Communications* **12**, 2964 (2021).
- [41] J. Holmes, D. Torodii, M. Balodis, M. Cordova, A. Hofstetter, F. Paruzzo, S. O. Nilsson Lill, E. Eriksson, P. Berruyer, B. Simões De Almeida, M. J. Quayle, S. T. Norberg, A. Svensk-Ankarberg, S. Schantz, and L. Emsley, Atomic-level structure of the amorphous drug Atuliflapon by NMR crystallography, *Faraday Discussions* , 10.1039.D4FD00078A (2024).
- [42] J. L. Guest, E. A. E. Bourne, M. A. Screen, M. R. Wilson, T. N. Pham, and P. Hodgkinson, The essential synergy of MD simulation and NMR in understanding amorphous drug forms, *Faraday Discussions* **255**, 325 (2025).
- [43] D. Torodii, M. Cordova, J. B. Holmes, P. Moutzouri, T. Casalini, S. O. Nilsson Lill, A. C. Pinon, C. S. Knee, A. Svensk Ankarberg, O. D. Putra, S. Schantz, and L. Emsley, Three-Dimensional Atomic-Level Structure of an Amorphous Glucagon-Like Peptide-1 Receptor Agonist, *Journal of the American Chemical Society* **147**, 17077 (2025).
- [44] J. Cuny, Y. Xie, C. J. Pickard, and A. A. Hassanali, *Ab Initio* Quality NMR Parameters in Solid-State Materials Using a High-Dimensional Neural-Network Representation, *Journal of Chemical Theory and Computation* **12**, 765 (2016).
- [45] F. M. Paruzzo, A. Hofstetter, F. Musil, S. De, M. Ceriotti, and L. Emsley, Chemical shifts in molecular solids by machine learning, *Nature Communications* **9**, 4501 (2018).
- [46] S. Liu, J. Li, K. C. Bennett, B. Ganoe, T. Stauch, M. Head-Gordon, A. Hexemer, D. Ushizima, and T. Head-Gordon, Multiresolution 3D-DenseNet for Chemical Shift Prediction in NMR Crystallography, *The Journal of Physical Chemistry Letters* **10**, 4558 (2019), publisher: American Chemical Society.
- [47] Z. Chaker, M. Salanne, J.-M. Delaite, and T. Charpentier, NMR shifts in aluminosilicate glasses *via* machine learning, *Physical Chemistry Chemical Physics* **21**, 21709 (2019).
- [48] P. A. Unzueta, C. S. Greenwell, and G. J. O. Beran, Predicting Density Functional Theory-Quality Nuclear Magnetic Resonance Chemical Shifts via  $\Delta$ -Machine Learning, *Journal of Chemical Theory and Computation* **17**, 826 (2021).
- [49] M. Cordova, E. A. Engel, A. Stefaniuk, F. Paruzzo, A. Hofstetter, M. Ceriotti, and L. Emsley, A Machine Learning Model of Chemical Shifts for Chemically and Structurally Diverse Molecular Solids, *The Journal of Physical Chemistry C* **126**, 16710 (2022).
- [50] J. Li, J. Liang, Z. Wang, A. L. Ptaszek, X. Liu, B. Ganoe, M. Head-Gordon, and T. Head-Gordon, Highly Accurate Prediction of NMR Chemical Shifts from Low-Level Quantum Mechanics Calculations Using Machine Learning, *Journal of Chemical Theory and Computation* **20**, 2152 (2024).
- [51] M. C. Venetos, M. Wen, and K. A. Persson, Machine Learning Full NMR Chemical Shift Tensors of Silicon Oxides with Equivariant Graph Neural Networks, *The Journal of Physical Chemistry A* **127**, 2388 (2023).
- [52] C. B. Mahmoud, L. A. M. Rosset, J. R. Yates, and V. L. Deringer, Graph-neural-network predictions of solid-state nmr parameters from spherical tensor decomposition, Preprint, arXiv:2412.15063 [cond-mat], <https://arxiv.org/abs/2412.15063> (2024), prepublished: 2024-12-19; accessed 2025-04-06.
- [53] Z. Li, B. Zhao, H. Zhang, and Y. Zhang, High-throughput calculations and machine learning modeling of  $^{17}\text{O}$  NMR in non-magnetic oxides, *Faraday Discussions* **255**, 72 (2025).
- [54] C. R. Groom, I. J. Bruno, M. P. Lightfoot, and S. C. Ward, The Cambridge Structural Database, *Acta Crystallographica Section B Structural Science, Crystal Engineering and Materials* **72**, 171 (2016).
- [55] E. A. Engel, A. Anelli, A. Hofstetter, F. Paruzzo, L. Emsley, and M. Ceriotti, A Bayesian approach to NMR crystal structure determination, *Physical Chemistry Chemical Physics* **21**, 23385 (2019).
- [56] K. P. Murphy, *Machine Learning - A Probabilistic Perspective*, Adaptive Computation and Machine Learning (MIT Press, Cambridge, 2014).
- [57] F. Musil, M. J. Willatt, M. A. Langovoy, and M. Ceriotti, Fast and Accurate Uncertainty Estimation in Chemical Machine Learning, *J. Chem. Theory Comput.* **15**, 906 (2019).
- [58] A. P. Bartók, R. Kondor, and G. Csányi, On representing chemical environments, *Physical Review B* **87**, 184115 (2013).
- [59] A. F. Harper, T. Huss, S. S. Köcher, and C. Scheurer, Tracking Li atoms in real-time with ultra-fast NMR simulations, *Faraday Discussions* **255**, 411 (2025).

- [60] V. Zaverkin, J. Netz, F. Zills, A. Köhn, and J. Kästner, Thermally Averaged Magnetic Anisotropy Tensors via Machine Learning Based on Gaussian Moments, *Journal of Chemical Theory and Computation* **18**, 1 (2022).
- [61] S. Pozdnyakov and M. Ceriotti, Smooth, exact rotational symmetrization for deep learning on point clouds, in *Advances in Neural Information Processing Systems*, Vol. 36, edited by A. Oh, T. Naumann, A. Globerson, K. Saenko, M. Hardt, and S. Levine (Curran Associates, Inc., 2023) pp. 79469–79501.
- [62] J. K. Harper and J. D. Hartman, Measuring and modeling anisotropy in the NMR of solids, *Magnetic Resonance in Chemistry* **62**, 124 (2024).
- [63] J. Herzfeld and A. E. Berger, Sideband intensities in NMR spectra of samples spinning at the magic angle, *The Journal of Chemical Physics* **73**, 6021 (1980).
- [64] W. T. Dixon, Spinning-sideband-free and spinning-sideband-only NMR spectra in spinning samples, *The Journal of Chemical Physics* **77**, 1800 (1982).
- [65] Z. Gan, High-resolution chemical shift and chemical shift anisotropy correlation in solids using slow magic angle spinning, *Journal of the American Chemical Society* **114**, 8307 (1992).
- [66] S. Gann, J. Baltisberger, and A. Pines, Dynamic-angle spinning without sidebands, *Chemical Physics Letters* **210**, 405 (1993).
- [67] O. N. Antzutkin, S. C. Shekar, and M. H. Levitt, Two-Dimensional Sideband Separation in Magic-Angle-Spinning NMR, *Journal of Magnetic Resonance, Series A* **115**, 7 (1995).
- [68] J. Meiler, PROSHIFT: Protein chemical shift prediction using artificial neural networks, *Journal of Biomolecular NMR* **26**, 25 (2003).
- [69] B. Han, Y. Liu, S. W. Ginzinger, and D. S. Wishart, SHIFTX2: Significantly improved protein chemical shift prediction, *Journal of Biomolecular NMR* **50**, 43 (2011).
- [70] G. Imbalzano, A. Anelli, D. Giofré, S. Klees, J. Behler, and M. Ceriotti, Automatic selection of atomic fingerprints and reference configurations for machine-learning potentials, *J. Chem. Phys.* **148**, 241730 (2018).
- [71] M. Kellner, J. B. Holmes, R. Rodriguez-Madrid, F. Viscosi, Y. Zhang, L. Emsley, and M. Ceriotti, A deep learning model for chemical shieldings in molecular organic solids including anisotropy, *Materials Cloud Archive 2025.X* (2025), draft; last updated 12 June 2025.
- [72] J. D. Hartman, S. Monaco, B. Schatschneider, and G. J. O. Beran, Fragment-based  $^{13}\text{C}$  nuclear magnetic resonance chemical shift predictions in molecular crystals: An alternative to planewave methods, *The Journal of Chemical Physics* **143**, 102809 (2015).
- [73] Metatensor Developers, Metatensor/Metatrain: Training and evaluating machine-learning models for atomistic systems, <https://github.com/metatensor/metatrain> (2025).
- [74] M. F. Langer, S. N. Pozdnyakov, and M. Ceriotti, Probing the effects of broken symmetries in machine learning, *Machine Learning: Science and Technology* **5**, 04LT01 (2024).
- [75] A. Grisafi, D. D. M. Wilkins, G. Csányi, and M. Ceriotti, Symmetry-Adapted Machine Learning for Tensorial Properties of Atomistic Systems, *Phys. Rev. Lett.* **120**, 036002 (2018).
- [76] U. Haeberlen, *High Resolution NMR in Solids: Selective Averaging*, *Advances in Magnetic Resonance* : Supplement No. 1 (Academic Press, New York, 1976).
- [77] F. A. L. Anet and D. J. O’Leary, The shielding tensor. Part I: Understanding its symmetry properties, *Concepts in Magnetic Resonance* **3**, 193 (1991).
- [78] J. C. Facelli, Chemical shift tensors: Theory and application to molecular structural problems, *Progress in Nuclear Magnetic Resonance Spectroscopy* **58**, 176 (2011).
- [79] R. P. Young, C. R. Lewis, C. Yang, L. Wang, J. K. Harper, and L. J. Mueller, TensorView: A software tool for displaying NMR tensors, *Magnetic Resonance in Chemistry* **57**, 211 (2019).
- [80] D. P. Kingma and J. Ba, Adam: A method for stochastic optimization, Preprint, arXiv:1412.6980 [cs]. <https://arxiv.org/abs/1412.6980> (2017), prepublished: 2017-01-30; accessed 2025-04-06.
- [81] P. Misof, P. Kessel, and J. E. Gerken, Equivariant neural tangent kernels, Preprint, arXiv:2406.06504 [cs]. <https://arxiv.org/abs/2406.06504> (2025), prepublished: 2025-01-31; accessed 2025-04-06.
- [82] J. E. Gerken and P. Kessel, Emergent equivariance in deep ensembles, Preprint, arXiv:2403.03103 [cs]. <https://arxiv.org/abs/2403.03103> (2024), prepublished: 2024-06-15; accessed 2025-04-06.
- [83] E. Hüllermeier and W. Waegeman, Aleatoric and epistemic uncertainty in machine learning: An introduction to concepts and methods, *Machine Learning* **110**, 457 (2021).
- [84] B. Lakshminarayanan, A. Pritzel, and C. Blundell, Simple and Scalable Predictive Uncertainty Estimation using Deep Ensembles, in *Advances in Neural Information Processing Systems*, Vol. 30, edited by I. Guyon, U. V. Luxburg, S. Bengio, H. Wallach, R. Fergus, S. Vishwanathan, and R. Garnett (Curran Associates, Inc., 2017).
- [85] A. E. Raftery, T. Gneiting, F. Balabdaoui, and M. Polakowski, Using Bayesian Model Averaging to Calibrate Forecast Ensembles, *Monthly Weather Review* **133**, 1155 (2005).
- [86] M. Kellner and M. Ceriotti, Uncertainty quantification by direct propagation of shallow ensembles, *Machine Learning: Science and Technology* **5**, 035006 (2024).
- [87] P. A. Unzueta, *Low-Cost Strategies for Predicting Accurate Density Functional Theory-Based Nuclear Magnetic Resonance Chemical Shifts*, Phd dissertation, University of California, Riverside (2022).
- [88] C. Guo, G. Pleiss, Y. Sun, and K. Q. Weinberger, On Calibration of Modern Neural Networks, in *Proceedings of the 34th International Conference on Machine Learning* (PMLR, 2017) pp. 1321–1330.
- [89] V. Kuleshov, N. Fenner, and S. Ermon, Accurate Uncertainties for Deep Learning Using Calibrated Regression, in *Proceedings of the 35th International Conference on Machine Learning* (PMLR, 2018) pp. 2796–2804.
- [90] P. Giannozzi, S. Baroni, N. Bonini, M. Calandra, R. Car, C. Cavazzoni, D. Ceresoli, G. L. Chiarotti, M. Cococcioni, I. Dabo, A. Dal Corso, S. de Gironcoli, S. Fabris, G. Fratesi, R. Gebauer, U. Gerstmann, C. Gougoussis, A. Kokalj, M. Lazzeri, L. Martin-Samos, N. Marzari, F. Mauri, R. Mazzarello, S. Paolini, A. Pasquarello, L. Paulatto, C. Sbraccia, S. Scandolo, G. Sclauzero, A. P. Seitsonen, A. Smogunov, P. Umari, and R. M. Wentzcovitch, Quantum espresso: a modular and open-source software project for quantum simulations of materials, *Journal of Physics: Condensed Matter* **21**, 395502 (19pp)

- (2009).
- [91] P. Giannozzi, O. Andreussi, T. Brumme, O. Bunau, M. B. Nardelli, M. Calandra, R. Car, C. Cavazzoni, D. Ceresoli, M. Cococcioni, N. Colonna, I. Carnimeo, A. D. Corso, S. de Gironcoli, P. Delugas, R. A. D. Jr, A. Ferretti, A. Floris, G. Fratesi, G. Fugallo, R. Gebauer, U. Gerstmann, F. Giustino, T. Gorni, J. Jia, M. Kawamura, H.-Y. Ko, A. Kokalj, E. Küçükbenli, M. Lazzeri, M. Marsili, N. Marzari, F. Mauri, N. L. Nguyen, H.-V. Nguyen, A. O. de-la Roza, L. Paulatto, S. Poncé, D. Rocca, R. Sabatini, B. Santra, M. Schlipf, A. P. Seitsonen, A. Smogunov, I. Timrov, T. Thonhauser, P. Umari, N. Vast, X. Wu, and S. Baroni, Advanced capabilities for materials modelling with quantum espresso, *Journal of Physics: Condensed Matter* **29**, 465901 (2017).
- [92] T. Gallagher, P. Alexander, P. Bryan, and G. L. Gilliland, Two Crystal Structures of the B1 Immunoglobulin-Binding Domain of Streptococcal Protein G and Comparison with NMR, *Biochemistry* **33**, 4721 (1994).
- [93] B. J. Wylie, W. T. Franks, D. T. Graesser, and C. M. Rienstra, Site-Specific  $^{13}\text{C}$  Chemical Shift Anisotropy Measurements in a Uniformly  $^{15}\text{N}$ ,  $^{13}\text{C}$ -Labeled Microcrystalline Protein by 3D Magic-Angle Spinning NMR Spectroscopy, *Journal of the American Chemical Society* **127**, 11946 (2005).
- [94] W. T. Franks, D. H. Zhou, B. J. Wylie, B. G. Money, D. T. Graesser, H. L. Frericks, G. Sahota, and C. M. Rienstra, Magic-Angle Spinning Solid-State NMR Spectroscopy of the B1 Immunoglobulin Binding Domain of Protein G (GB1):  $^{15}\text{N}$  and  $^{13}\text{C}$  Chemical Shift Assignments and Conformational Analysis, *Journal of the American Chemical Society* **127**, 12291 (2005).
- [95] G. Imbalzano, Y. Zhuang, V. Kapil, K. Rossi, E. A. Engel, F. Grasselli, and M. Ceriotti, Uncertainty estimation for molecular dynamics and sampling, *The Journal of Chemical Physics* **154**, 074102 (2021).
- [96] H. M. McConnell and C. H. Holm, Anisotropic Chemical Shielding and Nuclear Magnetic Relaxation in Liquids, *The Journal of Chemical Physics* **25**, 1289 (1956).
- [97] J. P. Perdew, K. Burke, and M. Ernzerhof, Generalized Gradient Approximation Made Simple, *Physical Review Letters* **77**, 3865 (1996).
- [98] F. Xu, W. Guo, F. Wang, L. Yao, H. Wang, F. Tang, Z. Gao, L. Zhang, W. E, Z.-Q. Tian, and J. Cheng, Toward a unified benchmark and framework for deep learning-based prediction of nuclear magnetic resonance chemical shifts, *Nature Computational Science*, 1 (2025), publisher: Nature Publishing Group.
- [99] C. M. Widdifield, N. Kaur, and K. M. N. Nguyen, NMR Crystallography Structure Determinations with  $^1\text{H}$  Chemical Shifts. GIPAW DFT Calculation Quality Can Be Substantially Degraded, but Nearly Identical Outputs Relative to Benchmark Computations Are Obtained: Why and So What?, *The Journal of Physical Chemistry A* **129**, 3722 (2025).

# Supplementary Information

## S1. DETAILED PREDICTION ACCURACIES OF SHIFTML3

We evaluate the accuracy of ShiftML3 on the CSD-test set described in the main text. In Table S1, we report the size of the training, validation and CSD-test set together with the mean average error (MAE), root-mean-squared-error (RMSE), the coefficient of determination ( $R^2$ ), and the standardized RMSE ( %) evaluation metrics of  $\sigma_{\text{iso}}$  predictions of ShiftML3 for all chemical species contained in *CSD-test*.

Table S1: Predicted accuracy of  $\sigma_{\text{iso}}$  of ShiftML2 (sML2) and ShiftML3 (sML3) on the *CSD-test* hold-out set

nucleus	N <sub>train</sub>	N <sub>validation</sub>	N <sub>test</sub>	MAE [ppm]		RMSE [ppm]		RMSE [%]		R <sup>2</sup>	
				sML2	sML3	sML2	sML3	sML2	sML3	sML2	sML3
<sup>1</sup> H	547,887	18,505	47,706	0.39	0.33	0.51	0.43	16	14	0.97	0.98
<sup>13</sup> C	437,529	16,971	43,435	3.15	1.58	4.63	2.32	9	5	0.99	1.00
<sup>15</sup> N	119,413	1,879	4,635	10.29	5.00	15.72	10.41	14	10	0.98	0.99
<sup>17</sup> O	135,305	3,272	8,058	16.11	7.51	22.96	11.45	13	6	0.98	1.00
<sup>19</sup> F	37,765	296	569	7.77	4.42	10.83	6.66	18	11	0.97	0.99
<sup>33</sup> S	30,500	386	1,084	34.35	15.05	53.34	26.34	35	17	0.88	0.97
<sup>31</sup> P	8,508	84	151	21.83	9.49	39.20	18.98	61	30	0.62	0.91
<sup>35</sup> Cl	25,608	188	569	17.40	10.44	23.85	15.11	21	13	0.96	0.98
<sup>23</sup> Na	1,138	9	5	7.64	4.09	8.10	4.61	100	57	0.00	0.68
<sup>43</sup> Ca	613	3	5	5.81	2.96	6.98	3.34	44	21	0.81	0.96
<sup>25</sup> Mg	283	3	7	10.69	3.68	14.55	5.49	58	22	0.66	0.95
<sup>39</sup> K	995	3	6	3.42	4.29	4.28	4.65	48	52	0.77	0.73

## S2. ROTATIONAL FLUCTUATIONS OF PET AND PET-ENSEMBLE

PET models learn the correct rotational behaviour of the targets via rotational augmentations. Langer and coworkers have investigated the effect relaxing exact rotational invariance to learned invariances, [74] and found that for realistic atomistic modelling tasks, this constraint can be safely relaxed. The remaining rotational fluctuations of the PET model and PET ensemble should however be carefully assessed for chemical shielding prediction tasks. Unlike the prediction of potential energies, or other structure wise global quantities, chemical shieldings are atom-wise properties. The common ansatz of predicting potential energies with neural networks, is by summing over local, per-atom terms. Shortcomings (imperfectly learned rotational invariance) of a non-invariant architecture might simply be compensated by error cancellation summing over atomic contributions. Since chemical shieldings and shielding tensors are exactly these local contribution (one prediction per atom), we study the effects of applying random rotations to structures and measuring the fluctuations of the predicted isotropic chemical shieldings. We apply 30 random rotations to each structure in the CSD test set and evaluate the standard deviation of the isotropic chemical shielding predictions. For a perfectly invariant model, these fluctuations should be exactly zero due to the invariance of the model. For an approximately invariant model, these predictions should be quite small, at most a fraction of the prediction RMSEs, such that they do not interfere with NMR crystal structure prediction workflows. In Table S2 we list rotational fluctuations, of ShiftML3 predictions across various chemical species and compare them with the rotational fluctuations of single PET models, highlighting the strongly reduced fluctuation of the ensemble of PET models that make ShiftML3.

We find that for most nuclei, ensemble uncertainty estimates are correlated with the rotational fluctuations. We evaluate the structure wise fluctuations of the RMSEs of the ShiftML3 predictions for CSD-test with respect to the GIPAW reference. To assess the effect of approximate invariance we also compute the fluctuations of the RMSE between all <sup>1</sup>H environments in a structure and its non-rotated structure. The mean fluctuation (mean of the standard deviation of fluctuations) of this RMSE across the CSD test set is 0.0065 ppm and the maximal fluctuation we find to be 0.0271 ppm.

Table S2: Average rotational fluctuations (average of all environment wise standard deviations applying 30 random rotations)  $\text{std}_{\text{rot}}[\sigma_{\text{iso}}]$  and maximal rotational fluctuation (of environment wise standard deviations) across all considered environment  $\text{max}_{\text{rot}}[\sigma_{\text{iso}}]$  of ShiftML3 predictions across the CSD-test set, of both the final *ensemble* model, as well as the individual committee models (single). All metrics are given in (ppm). *Single* is obtained by first evaluating each model on the hold-out test set and then averaging over the mean and max fluctuations of each model on the entire hold out set, whilst the *ensemble* values are obtained by first averaging the individual model predictions (computing the ShiftML3 model predictions) and then evaluating mean and max fluctuations on the hold out set.

nucleus	single		ensemble (ShiftML3)	
	$\text{std}_{\text{rot}}[\sigma_{\text{iso}}]$	$\text{max}_{\text{rot}}[\sigma_{\text{iso}}]$	$\text{std}_{\text{rot}}[\sigma_{\text{iso}}]$	$\text{max}_{\text{rot}}[\sigma_{\text{iso}}]$
$^1\text{H}$	0.41	1.78	0.06	0.23
$^{13}\text{C}$	1.19	7.13	0.14	0.71
$^{15}\text{N}$	2.57	23.49	0.29	1.57
$^{17}\text{O}$	3.98	43.35	0.45	2.22
$^{19}\text{F}$	2.27	9.09	0.26	0.70
$^{33}\text{S}$	5.28	36.90	0.59	3.13
$^{31}\text{P}$	2.82	19.81	0.33	1.49
$^{35}\text{Cl}$	4.73	22.13	0.50	2.03

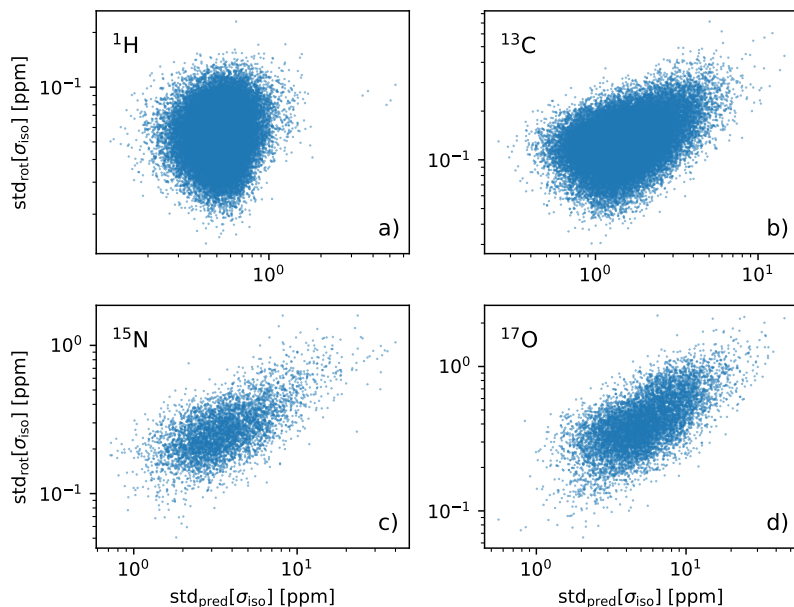


Figure S1: Correlations of uncertainty estimates  $\sigma_{\text{pred}}[\sigma_{\text{iso}}]$  across all atomic environments in the CSD-test set with the rotational fluctuations of the same environments  $\text{std}_{\text{rot}}[\sigma_{\text{iso}}]$ , for  $^1\text{H}$  (a),  $^{13}\text{C}$  (b),  $^{15}\text{N}$  (c) and  $^{17}\text{O}$  (d).

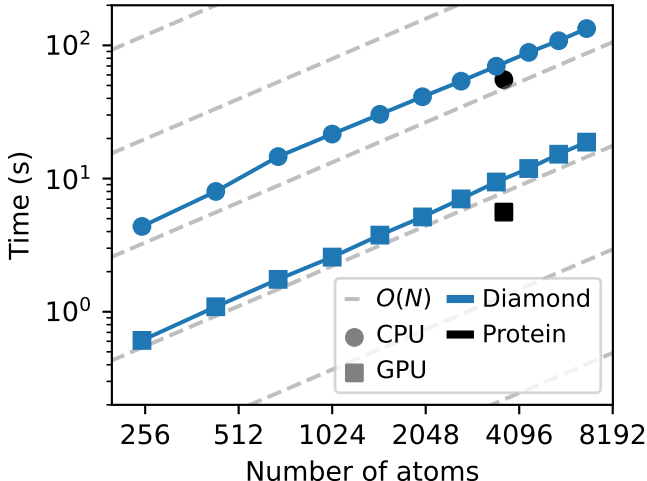
### S3. MODEL EVALUATION TIMINGS

We benchmark the evaluation time of the ShiftML3 model. All benchmark timings are obtained via the ASE interface of the ShiftML library. We report timings that include setting up the ASE calculator once and then computing chemical shielding tensors for a series of structures. We believe that this protocol reflects most accurately the evaluation timings for a common NMR crystallography workflow. The timings via the ASE interface include also the neighbour list construction. The ASE interface does not support batched evaluations, or efficient parallelization over ensemble models for smaller system sizes. We report CPU-only and CPU+GPU timings. We report evaluation times on a Lenovo workstation with a AMD Ryzen Threadripper PRO 3955WX CPU with 16 cores. CPU+GPU timings are obtained on the same workstation, using a NVIDIA GeForce RTX 4070 Ti-super consumer GPU, which is representative of a configuration that does not require access to high-end AI-dedicated hardware. As shown in Table S3, even a low-end GPU accelerates by 4x-6x the evaluation of structures with the size of typical small-molecule

Table S3: Average timing of the ShiftML3 model for evaluating chemical shieldings on CPU or GPU. We also list the average number of atoms  $\bar{N}_{\text{atoms}}$  in the *CSD-test* hold-out test set.

Set	Time per struct. [s]		$\bar{N}_{\text{atoms}}$
	CPU/GPU		
<i>CSD-test</i>	0.81/0.23		125

Figure S2: Scaling of the inference time of the ShiftML3 model with system size. Blue lines indicate timings for diamond supercells of increasing size. Black markers are the evaluation times of the 1PGA protein crystal. Grey lines correspond to linear scaling.



pharmaceuticals. The acceleration is also evident at larger system sizes: the scaling of the ShiftML3 model for diamond supercells of increasing size is almost perfectly linear, and there is an order-of-magnitude acceleration when using a GPU (Fig. S2). These timings are also representative of large biomolecules, as hinted at by the inference timings for the protein crystal of 1PGA [92], the B1 immunoglobulin-binding domain of the streptococcal protein G with 56 amino acid residues and 3,656 atoms in the conventional cell (also shown in Fig. S2). 1PGA was a target of several solid-state NMR studies [93, 94] and therefore lies well within the range of atomistic systems of interest for which chemical shielding predictions may complement experimental studies. A computation of chemical shieldings for this protein takes 5.6 s using the GPU. Moving to even larger systems, we find that on the consumer GPU used for benchmarking with 16GB of VRAM, we can predict  $^{13}\text{C}$  shieldings in diamond supercells of up to 16,000 atoms before exhausting the graphics card video memory, demonstrating the memory efficiency of ShiftML3.

#### S4. IMPLEMENTATION

To simplify usage of ShiftML3 for inference, we make it available with an easy-to-install Python package, released together with this publication. ShiftML is available from the Python Package Index PyPi and can be easily installed with

```
pip install shiftml
```

The ShiftML3 model integrates into existing materials modelling and crystal structure prediction workflows via the atomic simulation environment. Chemical shielding predictions can be obtained by initializing an ASE calculator object and reading in the geometry file in one of the various supported file formats. Once the calculator is initialized, the model weights are automatically downloaded and loaded by the model. A minimalistic usage example is given below, and a more thorough tutorial is available at <http://atomistic-cookbook.org/shiftml/shiftml-example.html>.

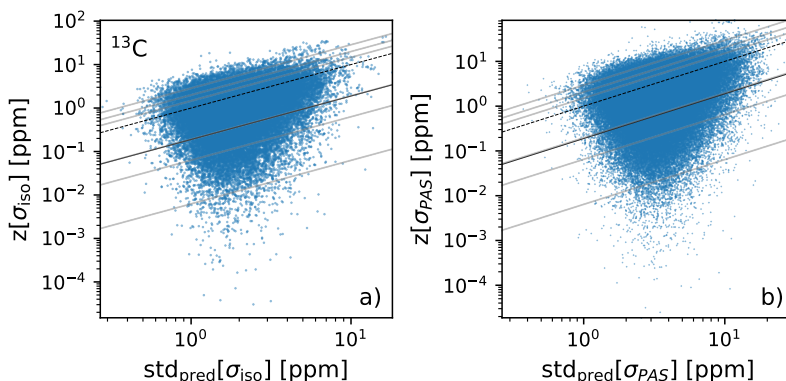


Figure S3: Predicted uncertainties of  $^{13}\text{C}$  isotropic chemical shieldings  $\text{std}_{\text{pred}}[\sigma_{\text{iso}}]$  vs the actual prediction errors  $z[\sigma_{\text{iso}}]$  (a) and predicted uncertainties of the corresponding principal components  $\text{std}_{\text{pred}}[\sigma_{\text{PAS}}]$  vs the actual component prediction errors  $z[\sigma_{\text{PAS}}]$  (b). The grey lines indicate quantiles of the expected error distribution for a given predicted uncertainty values and are intended to guide the readers eye: For example, on the test set, for well calibrated uncertainty estimates there should be 90% of the samples between the two outmost lines as they correspond to quantile lines of 95% and 5% of the folded log normal distribution.

```

from ase.build import bulk
from shiftml.ase import ShiftML

frame = bulk("C", "diamond", a=3.566)
model = ShiftML("ShiftML3")

Ypred = model.get_cs_tensor(frame)

```

## S5. UNCERTAINTY QUANTIFICATION AND CALIBRATION

The ensemble uncertainty estimates we obtain are miscalibrated (as it is often the case [88, 89] in uncertainty quantification schemes for neural networks), i.e. the uncertainty estimates across all samples of a hold-out validation or test set model uncertainty estimates are systematically over- or underconfident. It is possible to rescale the uncertainty estimates, and correct the miscalibration by computing a global, input-independent scaling factor [57, 95] (an empirical correction that is similar in spirit to *temperature scaling*, [88] a classical method in uncertainty quantification). The scaling factor can be computed via a closed form expression, that can be derived by maximizing the Gaussian negative log likelihood on a hold out test set given predicted uncertainties and squared prediction errors  $z_i^2(A)$ .

$$\alpha^2 = \sum_{i=1}^{N_{\text{samples}}} \frac{z_i^2(A)}{\sigma_{i,\text{pred}}^2(A)} \quad (2)$$

The final, calibrated, uncertainties are then obtained as  $\alpha^2 \sigma_{\text{pred}}^2(A)$  - although in practice we scale the ensemble members around their mean, which simplifies uncertainty propagation. [86] We find that for isotropic chemical shieldings and shielding tensor principal components the calibration factors  $\alpha$  are moderate and always close to 1, indicating that the ShiftML3 ensemble uncertainty estimates, are already well calibrated.

We evaluate the uncertainty estimates of the ShiftML3 model on the CSD-test set and plot the predicted uncertainties of  $^{13}\text{C}$  shieldings vs the actual prediction errors. In Fig. S3 we show parity plots of predicted and calibrated uncertainties of the ShiftML3 model and the actual errors on a hold out test set.

## S6. ANTISYMMETRIC CHEMICAL SHIELDING TENSOR PREDICTIONS

The chemical shielding tensor can be decomposed into a symmetric and antisymmetric part (eq. 3):

$$\sigma = \sigma_{\text{sym}} + \sigma_{\text{antisym}} = \frac{1}{2}(\sigma + \sigma^T) + \frac{1}{2}(\sigma - \sigma^T) \quad (3)$$

Only the symmetric part enters directly into the NMR spectrum, whilst the antisymmetric part effects relaxation times. [96] Therefore, in the main part of this manuscript we have focussed on evaluating and utilizing the CSA,  $\sigma_{\text{PAS}}$  which are the principal components of  $\sigma_{\text{sym}}$ . ShiftML3 can predict the full chemical shielding tensor, containing symmetric and antisymmetric parts. In Figure S4 we show parity plots of the symmetric and antisymmetric components  $\sigma_{ij,\text{sym}}$  and  $\sigma_{ij,\text{antisym}}$  of the  $^{13}\text{C}$  and  $^{17}\text{O}$  chemical shielding tensors.

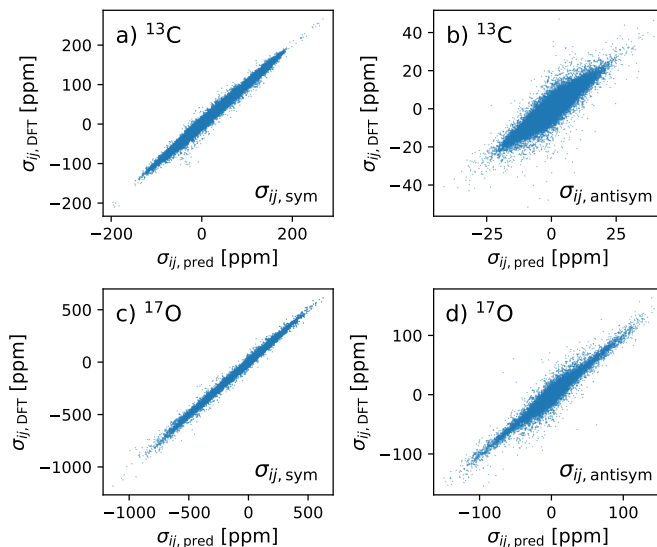


Figure S4: Parity plots of symmetric and antisymmetric chemical shielding tensor components  $\sigma_{ij,\text{sym}}$ ,  $\sigma_{ij,\text{antisym}}$  for  $^{13}\text{C}$  (a,b) and  $^{17}\text{O}$  (c,d) comparing the values predicted with ShiftML3 and those computed with DFT.

In Table S4 we list the prediction accuracies of ShiftML on CSD-test separately on antisymmetric and symmetric components of the chemical shielding tensor.

Table S4: Prediction accuracies RMSEs (ppm) and normalized prediction accuracies RMSE/std (%) of ShiftML3 of the components of the symmetric  $\sigma_{ij,\text{sym}}$  and antisymmetric shielding tensor  $\sigma_{ij,\text{antisym}}$ .

nucleus	$\sigma_{ij,\text{sym}}$		$\sigma_{ij,\text{antisym}}$	
	[ppm]	[%]	[ppm]	[%]
$^1\text{H}$	0.72	6	0.52	57
$^{13}\text{C}$	3.08	5	2.28	41
$^{15}\text{N}$	10.75	11	5.98	47
$^{17}\text{O}$	12.09	7	7.82	27
$^{19}\text{F}$	6.28	5	3.35	39
$^{33}\text{S}$	30.37	18	18.10	52
$^{31}\text{P}$	18.73	14	11.02	72
$^{35}\text{Cl}$	15.32	5	9.57	47
$^{23}\text{Na}$	4.01	2	1.58	81
$^{43}\text{Ca}$	3.85	1	1.31	29
$^{25}\text{Mg}$	9.79	3	4.55	39
$^{39}\text{K}$	3.95	1	2.05	67

Figure S5 shows that the symmetric and antisymmetric tensor components (for nuclei like  $^{13}\text{C}$  and  $^{17}\text{O}$ ) have similar absolute prediction errors. However, because the antisymmetric values span a much smaller range, their relative errors are much larger than those of the symmetric components.

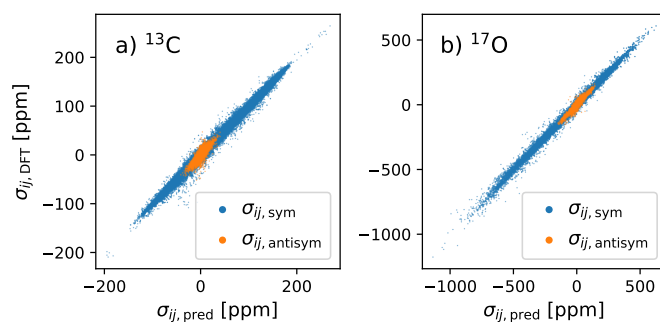


Figure S5: Parity plots of symmetric and antisymmetric chemical shielding tensor components  $\sigma_{ij, \text{sym}}$ ,  $\sigma_{ij, \text{antisym}}$  for  $^{13}\text{C}$  (a) and  $^{17}\text{O}$  (b) - combined parity plots.

In Figure. S6 we show parity plots of symmetric shielding tensor component predictions and principal tensor component predictions.

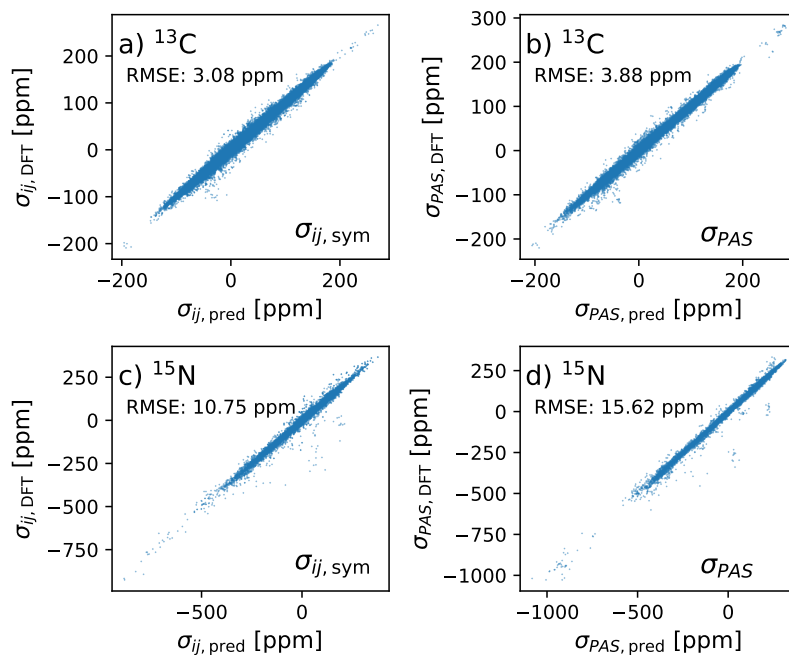


Figure S6: Parity plots of principal tensors components  $\sigma_{PAS}$  and symmetric tensor components  $\sigma_{ij}$  for  $^{13}\text{C}$  (a,b) and  $^{15}\text{N}$  (c,d)

## S7. DETAILS OF EXPERIMENTAL BENCHMARK EVALUATIONS

Evaluation of  $^1\text{H}$  was done on the same 13 structures where ShiftML2 was evaluated [49] on the same geometry optimized structures. Predicted shieldings of methyl or primary amine groups were averaged out accounting for rapid rotation, resulting in the averaged sites have equivalent chemical shielding. Ambiguous experimental assignments were solved by iterating along all possible permutations of those unassigned shifts and taking the assignment with the lowest RMSE between predicted and experimental chemical shift such as for methylene groups. Only the permutation with the lowest RMSE entered the global linear regression. We note that the reported RMSE comparing prediction to experiment for ShiftML2 is modestly different than the original work. This difference originates from the use of a global regression as compared to on-the-fly regression used in the original work. For  $^{13}\text{C}$  and  $^{15}\text{N}$ , the accuracy was evaluated from the benchmark consisting of 36 structures from Ramos *et al.* [14] on geometries optimized

on the PBE-D3(BJ)level of theory [97]. For the carbon CSA parameters, we used the benchmark consisting of 19 structures from Hartman *et al.* [72]

Table S5: RMSE and Linear regression parameters are for the DFT, ShiftML2, and ShiftML3 prediction and experimental chemical shifts from the respective benchmark.

Nucleus	Method	RMSE	Slope	Intercept
$^1\text{H}$ iso	ShiftML2	0.59	-0.8985	27.86
	ShiftML3	0.53	-0.9024	28.05
	DFT	0.49	-0.8902	27.58
$^{13}\text{C}$ iso	ShiftML2	2.91	-0.9667	165.07
	ShiftML3	2.44	-0.9732	166.23
	DFT	2.34	-0.9736	166.06
$^{15}\text{N}$ iso	ShiftML2	14.03	-1.0556	184.82
	ShiftML3	7.24	-1.025	183.34
	DFT	5.85	-1.0137	181.77
$^{13}\text{C}$ PAS	ShiftML3	5.2	-0.9576	164.84
	DFT	5.85	-0.9525	164.27

## S8. COMPARING SHIFTML3 WITH OTHER MACHINE LEARNING MODELS FOR CHEMICAL SHIELDING PREDICTION

A direct comparison of the ShiftML3 prediction accuracies with ShiftML2 reveals that it is more accurate for predicting isotropic chemical shieldings across all relevant elements. To the best of our knowledge, no other machine learning model has been trained on the last iteration of the ShiftML datasets, including thermally distorted structures and additional chemical elements. Unzueta *et al.* trained GNN models [87] and Liu and coworkers a multiresolution 3D-DenseNet architecture on the CSD-2K dataset [46], an early iteration of the ShiftML training sets. An alternative model construction strategy is the NMRNet from Xu and coworkers, that finetuned a transformer model for the chemical shielding prediction in liquids on the CSD-2K set [98]. All three works report evaluation accuracies on the CSD-500 set, a set of DFT relaxed organic crystals, containing at most H,C,N and O. Unfortunately the number of shared structures between the *CSD-test* and the CSD-500 test set is too small (about 10 structures) to make direct comparisons between the accuracies of ShiftML3 and other neural network architectures. Shielding computations are highly sensitive to k-space discretization and choice of pseudopotentials [99]. CSD-2K/CSD-500 was computed with other DFT convergence parameters than the ShiftML2/ShiftML3 dataset, hampering severely a direct comparison between all models - we regularly find that shielding values from computations employing different, yet reasonable convergence parameters, differ (in terms of their RMSEs) nearly as much as the ShiftML3 predicted shieldings differ from the CSD test reference calculations. Instead, we evaluate ShiftML2 and ShiftML3 on 351 structures in our test set that only contain H,C,N,O and are not MD distorted structures (containing 7536  $^1\text{H}$ , 6546  $^{13}\text{C}$ , 665  $^{15}\text{N}$  and 1311  $^{17}\text{O}$  test environments) and compare their relative improvements in accuracies against the other models, to give some context to the gains in accuracy we achieve with ShiftML3. In Table S6, we compare prediction accuracies of the original ShiftML1.0 model, Unzueta’s ensemble of GNNs, Liu’s MR-3D-DenseNet and compare them with the prediction accuracies of ShiftML2 and ShiftML3 on the H,C,N,O-relaxed subselection of the CSD-test set.

Table S6: Test set RMSEs (ppm) of the original ShiftML1.0 model (KRR [45]), Unzueta’s GNNs (GNN [87]) and Liu’s MR-3D-DenseNet (DenseNet [46]) and Xu’s NMRNet (NMRNet [98]) on the CSD-500 test set. We compare these values with the prediction accuracies of ShiftML2 (sML2) and ShiftML3 (sML3) on a comparable subset of the CSD test set. Note that KRR, GNN, DenseNet and NMRNet are evaluated on the CSD-500 test set. As discussed in the text, due to the small overlap of CSD-500 and the CSD test set, we choose to evaluate sML2 and sML3 on a subset of the CSD test set containing only H,C,N,O structures that are geometry relaxed. (\*) Denotes, that the results of sML2 and sML3 were obtained on that subselection.

Nucleus	KRR	GNN	DenseNet	NMRNet	sML2*	sML3*
<sup>1</sup> H	0.49	0.49	0.37	0.35	0.47	0.39
<sup>13</sup> C	4.3	4.06	3.3	3.21	4.07	1.97
<sup>15</sup> N	13.3	9.90	10.2	9.45	12.52	5.71
<sup>17</sup> O	17.7	14.4	15.3	13.03	19.50	9.91